Fault-induced delayed voltage recovery in a long inhomogeneous power-distribution feeder

Irina Stolbova, Scott Backhaus, and Michael Chertkov

Fault Induced Delayed Voltage Recovery
in a Long Inhomogeneous Power Distribution Feeder

Irina Stolbova [a], Scott Backhaus [b,c], and Michael Chertkov [d,c]

[a] Moscow Institute of Physics and Technology, Dolgoprudnyj, Moscow Regiona 141700, Russia
[b] Materials, Physics & Applications Division, Los Alamos National Laboratory, NM 87545, USA
[c] New Mexico Consortium, Los Alamos, NM 87544, USA and
[d] Theoretical Division and Center for Nonlinear Studies, Los Alamos National Laboratory, NM 87545, USA

We analyze the dynamics of a distribution circuit loaded with many induction motor and subjected to sudden changes in voltage at the beginning of the circuit. As opposed to earlier work [1], the motors are disordered, i.e. the mechanical torque applied to the motors varies in a random manner along the circuit. In spite of the disorder, many of the qualitative features of a homogenous circuit persist, e.g. long-range motor-motor interactions mediated by circuit voltage and electrical power flows result in coexistence of the spatially-extended and propagating normal and stalled phases. We also observed a new phenomenon absent in the case without inhomogeneity/disorder. Specifically, transition front between the normal and stalled phases becomes somewhat random, even when the front is moving very slowly or is even stationary. Motors within the blurred domain appears in a normal or stalled state depending on the local configuration of the disorder. We quantify effects of the disorder and discuss statistics of distribution dynamics, e.g. the front position and width, total active/reactive consumption of the feeder and maximum clearing time.

I. INTRODUCTION

The majority of transient and dynamical stability studies in power systems focuses on high voltage transmission grids where detailed models of the generators and transmission lines are used. In contrast, these studies use crude aggregations of individual small loads to model aggregate load dynamics. Recent years have seen an increased emphasis on dynamical load models [2, 3] for several reasons. First, transmission networks are being pushed harder and operated closer to their dynamical stability limits, and the uncertainty introduced by inaccurate linear dynamical load models presents an unacceptable operating risk [4]. Second, collective nonlinear dynamical load behaviors such as induction motor stalling and Fault-Induced Delayed Voltage Recovery (FIDVR) are being excited by seemingly typical transmission grid behavior such as normal fault clearing [5, 6].

In FIDVR, a short-lived but significant perturbation created by a transmission fault synchronizes the dynamical behavior of a large fraction of individual induction motor loads, and the ensuing collective dynamics induce a voltage collapse-like event that propagates to the transmission grid. Complicating the situation further, the future will likely see the introduction of many new "smart" consumer devices that include local controllers making decisions based upon local measurements. The actions of these independent and potentially stochastic load controls will yield new dynamics. There are no tools that can predict the collective effect of these dynamics and the potential impact on transmission grids. The example of FIDVR demonstrates the importance of understanding and modeling emergent collective effects in distribution dynamics for modeling of transmission grid dynamics. This work extends a model of distribution dynamics [1, 7] to study the impact of inhomogeneity in distribution circuit loading on the FIDVR dynamics mentioned above.

Diversity of distribution circuits makes detailed, component-by-component modeling of the many config-urations very difficult. Even if modeling of the family of such configurations were performed, it is not clear that the results could be understood or displayed in way that enables intuitive interpretation and understanding. Instead, we adopt the model of [7] and [1] where the distribution circuit power flows and load dynamics are represented as a continuum system and model the spatiotemporal dynamics using Partial Differential Equations (PDE). Similar approaches have been used to model dynamical effects in transmission grids [8, 9]. This PDE approach reveals the nontrivial interplay of the dynamics of loads via the spatial coupling provided by power flows over the electrical network. In [1], this approach was used to reveal the qualitative behavior of FIDVR dynamics in a uniformly-loaded distribution circuit, and in [10] this approach was used to explore new equilibrium states of a distribution circuit with a spatially-uniform installation of actively-controlled photovoltaic inverters. In both of these cases, the structure of the PDE reveals the important long-range interactions between local load behavior (dynamic or static) mediated by the power flows along the distribution circuit.

In this manuscript, we extend the work of [1] by investigating the effects of spatially inhomogeneous induction motor loading. Variation in loading is expected to modify the behavior of FIDVR dynamics, however, both the qualitative and quantitative effects are not clear. Pockets of high or low induction motor load could locally arrest or enhance the propagation of a FIDVR event, but long-range effects are also possible. We create realizations of circuit loadings using spatially-correlated Gaussian distribution of load parameters and study the behavior of the FIDVR dynamics as a function of the amplitude of the load disorder and the correlation length. From these studies, we find that, at least for relatively low amplitude and spatially short-correlated disorder, the effects on FIDVR dynamics are local. This conclusion has important implications for control, specifically, that a control scheme for eliminating or correcting disruptive FIDVR events is not strongly dependent on the details of the induction motor loading.
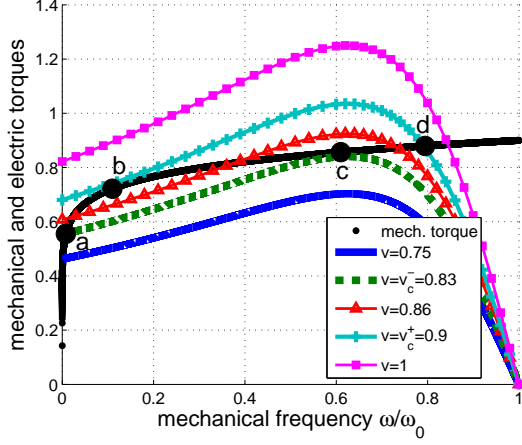
FIG. 1: Electric and mechanical torques as functions of the mechanical frequency ω/ω_0 for a range of motor terminal voltages v, reference mechanical torque $T_0 = 0.32$, and $\alpha = 0.1$. For the $v = 0.86$ electrical torque curve (red triangles), there are three equilibrium solutions indicated by intersections with the mechanical torque curve (black solid line). The solution with the highest ω/ω_0 is the "normal" stable solution with the induction motor rotating near the grid frequency ω_0. The "stalled-state" with $\omega/\omega_0 \simeq 0$ is also stable while the intermediate solution is unstable. For $v > v_c^+ = 0.9$ (light blue line with plus signs), there is only one solution corresponding to the normal state. For $v < v_c^- = 0.83$ (green dashed line), there is only one solution corresponding to the stalled state. The points (a, b, c, d) correspond to the same labels in Fig. 2.

The rest of the manuscript is organized as follows. Section II introduces the PDE model of distribution dynamics and load inhomogeneity and briefly describes the numerical methods used to integrate the PDE model. Section III presents the results of numerically integrating the PDE model with different types of load inhomogeneity, parameterized by the amplitude and the correlation length of the disorder, on different dynamical transients. Finally, Section IV provides some conclusions and potential areas for future work.

II. TECHNICAL INTRODUCTION

A. Dynamics of an Individual Motor

We adopt the model of induction motor load and dynamics from [11]. Here, we only describe the features of inductions motors that are important for the remainder of this manuscript. The real (P) and reactive (Q) powers drawn by and induction motor are

$$P = \frac{sR_m v^2}{R_m^2 + s^2 X_m^2}, \tag{1}$$

$$Q = \frac{s^2 X_m v^2}{R_m^2 + s^2 X_m^2}, \tag{2}$$

where $s = 1 - \omega/\omega_0$ is the slip of the motor's rotational frequency ω relative to the grid frequency ω_0 ($0 \le s < 1$); v
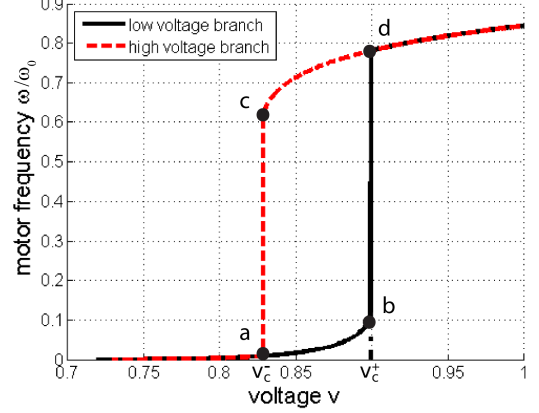

FIG. 2: Hysteretic behavior of an induction motor stable steady states in Fig. 1 as the voltage v at its terminals is varied. The dashed red (solid black) curves indicate the path of equilibrium states as the voltage v is decreased (increased) starting from the high-voltage normal (low-voltage stalled) state. The vertical lines at the spinodal voltages $v_c^\pm$ indicated the abrupt hysteretic transitions between states. $v_c^\pm$ correspond to the same labels in the legend of Fig. 1. The points (a, b, c, d) correspond to the states where the motor must make transitions from normal to stalled ($c \to a$) and from stalled to normal ($b \to d$).

is the voltage at the motor terminals; and X_m and R_m are internal reactance and resistance of the motor, respectively. Typically, $R_m/X_m = 0.1 \div 0.5$.

The real power load P creates an electric torque on the induction motor shaft which is countered by a mechanical load torque. Any imbalance between these torques results in an angular acceleration of the motor's rotational inertia M, i.e.

$$M\frac{d}{dt}\omega = \frac{P}{\omega_0} - T_0 \left(\frac{\omega}{\omega_0}\right)^\alpha. \tag{3}$$

Here T_0 is a reference mechanical torque and α is indicative of different types of mechanical loads with $\alpha = 1$ typical of fan loads and $\alpha < 1$ typical of air-conditioning or other compressor loads. If $\alpha < \alpha_c \simeq 1$ and T_0 are fixed, there exist three steady solutions of Eqs. (1,3) when v is in a range between two spinodal voltages v_c^- and v_c^+. Figure 1 displays the mechanical torque (black curve) and the electrical torque (colored curves) for different values of v. For a mid-range voltage of 0.86 (red triangles), the mechanical and electrical torque curves intersect for three values of ω/ω_0 defining three steady solutions. For the high and low ω/ω_0 solutions, the torque balance for small deviations away from steady solution push ω/ω_0 back to the steady state. The opposite is true for the mid-range ω/ω_0 solution making it unstable to small deviations.

From Fig. 1, it is clear that small changes in v in the vicinity of v_c^+ and v_c^- can lead to drastic and hysteretic changes in ω resulting in a large changes in the motor's P and Q (via Eqs. 1 and 2). These hysteretic changes will be coupled back to the dynamics in Eq. (3) via the power flow equations in Section II B [1]. This hysteresis and coupling can be affected

by inhomogeneity in loading, and these effects are explored in the remainder of this manuscript.

The effect of the hysteresis is cleanly displayed in Fig. 2 where the ω/ω_0 for two stable steady states is plotted versus the motor terminal voltage v. Starting in the high-voltage normal state (say $v \sim 1$), v can be slowly decreased along the dashed red curve passing through state d. Further decreasing v to state c, the "normal" state (i.e. the state with high ω/ω_0 suddenly disappears and the motor makes a transition to the "stalled" state at a. Similarly, if we start from the low-voltage stalled state (say $v \sim 0.75$ on the black curve) and v is increased slowly through state a to b, the stalled state disappears and the motor makes a transition to the normal state at d. For reference, the states (a, b, c, d) are also marked in Fig. 1, and the same hysteresis loop can be traced out there. The voltages v_c^+ and v_c^- depend on induction motor parameters, and disorder in these parameters will result in neighboring segments of the circuit making state transitions at different times. The discreteness of the transitions and the large changes in ω/ω_0, P, and Q will significantly amplify the even a small amount of disorder.

B. Continuum Model of Distribution Dynamics

The derivation of the continuous form of the DistFlow equations is described in [7]. Here, we only summarize the results that are important to the rest of this manuscript. The evolution of the real (ρ) and reactive (ϕ) line flows is caused by loads or line losses, i.e.

$$\partial_z \rho = -p - r\frac{\rho^2 + \phi^2}{v^2}, \tag{4}$$

$$\partial_z \phi = -q - x\frac{\rho^2 + \phi^2}{v^2}. \tag{5}$$

Here z is the coordinate along the distribution circuit, r, x are the per-unit-length resistance and reactance densities of the lines (assumed independent of z) and $p(z)$ and $q(z)$ are the local densities of real and reactive powers consumed by the density of the spatially continuous distribution of motors [7] at the position $z \in [0; L]$. The power flows ρ and ϕ are related to the voltage at the same position according to [7]

$$\partial_z v = -\frac{r\rho + x\phi}{v}. \tag{6}$$

The load densities $p(z)$ and $q(z)$ in Eqs. (4,5) are related to $\omega(z)$ and $v(z)$ through the density versions of Eqs. (1,2,3)

$$\mu \frac{d}{dt}\omega = \frac{p}{\omega_0} - \tau_0 \left(\frac{\omega}{\omega_0}\right)^\alpha, \tag{7}$$

$$p = \frac{s r_m v^2}{r_m^2 + s^2 x_m^2}, \tag{8}$$

$$q = \frac{s^2 x_m}{r_m^2 + s^2 x_m^2} v^2, \tag{9}$$

where the conversion to continuous form consists of replacing X_m, R_m and P, Q, T_0, M by the respective densities x_m, r_m

and p, q, τ_0, and μ. The new boundary conditions are

$$v(0) = v_0, \quad \rho(L) = \phi(L) = 0. \tag{10}$$

Eqs. (4-10) form our PDE model of a distribution feeder loaded with induction motors.

C. Model of Disorder

Analysis in [1] assumed that all of the induction motor parameters τ_0 are constant, i.e. the circuit is uniformly loaded with identical induction motors all serving identical loads. However, loading in distribution circuits is inhomogeneous and variable depending on, e.g., the time of day or environmental conditions. We relax the assumption of uniform loading by introducing load inhomogeneity by making τ_0 a random Gaussian variable centered on $\bar{\tau}_0$ (i.e. $\bar{\tau}_0 = \mathbb{E}[\tau_0(z)]$). Deviations from the mean $\delta(z) = \tau_0(z) - \bar{\tau}_0$ are statistically homogeneous with the covariance, $\mathbb{E}[\delta(z_1)\delta(z_2)] = (\tau_0\Delta)^2 \exp(-|z_1 - z_2|/z_d)$. The amplitude of the the disorder, as well as the correlation scale of the disorder are assumed small, $\Delta \ll 1$, $z_d/L \ll 1$, where L stands for the length of the feeder. The Gaussian model is the simplest and most natural spatially smooth and two parametric (amplitude and correlation length) model of the disorder. To implement the Gaussian finite correlated model of the inhomogeneity/disorder in the simulations of Eqs. (4-10), one sets up the spatial step size which is much smaller than the disorder's correlation length, z_d. The spatial step used in the simulation was $2.5 * 10^{-4}$ vs. $5 * 10^{-3}$ used for the minimum value of the correlation length.

Note that the motor shaft angle-dependent torque in reciprocating compressors is an effect that can lead to a higher likelihood of stalling as compared to a scroll-type compressor for the same average mechanical torque. The model of the individual motors we are using does not capture this effect and our use of DistFlow power flow equations precludes any representation electrical voltage phase. Although we believe (in accordance with what is described above) that the spatial disorder in the motor mechanical torques to arise from simple differences in motor types and loading, the disorder could also represent relative phase of the motor shaft angle and the voltage phase.

D. Numerical Simulation Approach

Eqs. (4-10) are integrated using the following iterative procedure (see [1] for details). For given current values of p and q, the discretized version of Eqs. (4,5,6) are solved by a shooting method, i.e. using the fixed v_0 from Eq. 10, $\rho(0)$ and $\phi(0)$ are adjusted until the spatial integration of the time-independent equations accurately recreates the boundary conditions in Eq. 10 at $z = L$. Using this voltage profile, the motors' ω are updated using a time-discretized version of Eq. (7). Using the new values of ω, the parameters s, p and q are updated using Eqs. (8,9) and the process repeats. In the simulations we assume that $\alpha = 0.1$, $x_m = 0.4$, $r_m = 0.15$, $r = 0.5$, $x = 0.5$, $L = 0.5$, $\mu = 0.1$, $w_0 = 1$ and $\bar{\tau}_0 = 0.9$.

III. NUMERICAL EXPERIMENTS: RESULTS

Eqs. (4-10) are studied numerically under a range conditions:

(S) Steady-state conditions—a constant $v_0=1$ is applied.

(A) Stalling front dynamics—starting from the previous steady-state conditions, v_0 is suddenly lowered by a range of Δv's and the dynamics of the motor stalling front is studied.

(B) Restoration front dynamics—starting from a fully stalled condition (i.e. $v_0 < 1$ and all motors on the low voltage branch of Fig. 2), v_0 is suddenly raised to 1.0, and the dynamics of motor restoration front is studied.

(C) Fault-clearing dynamics—A fault clearing perturbation is emulated by combining case A and case B. Starting from the steady-state condition from S, v_0 is lowered by Δv for time τ_{cl} to create a stalling front. After τ_{cl}, v_0 is subsequently restored to 1.0, and the restoration is studied. Our goal is to determine how the disorder in τ_0 affects the maximum fault clearing time, i.e. the longest the fault can stay on while the all of the motors on the circuit recover to the high-voltage branch in Fig. 2.

In each study, statistics are gathered over many samples of the distribution of motor and feeder disorder, i.e. Δ and z_d. For each simulated sample in case A and B, the following data is analyzed:

- The active and reactive power flows at $z = 0$, $\rho(0)$ and $\phi(0)$;

- The position of the front z_f and the width the front, z_w.

For case (C), the maximum fault clearing time τ_{cl} is found that still allows the circuit to recover to a fully normal state. The goal of these studies is to quantify the effect of disorder effect on statistics of these data. Aimed to test sensitivity of the results to the parameters of the disorder, Δ and z_d, were varied in our numerical experiments.

A. Case S—"Normal" Steady-State Solution

In real systems, motor stalling is observed to occur in as little time at 50 ms to as long as a few 100 ms. Typical fault clearing times can span a similar range of time scales depending on the design of the system. For example, we estimate that a typical stalling time of a 0.75KW 3-phase, wye-connected, squirrel cage 4 pole induction motor with the moment of inertia $M = 0.05 kg/m^2$ is $\approx 50 - 100 ms$. (See e.g. Appendix B of [12] for description of parameters of practical induction motors.) Therefore for a feeder containing these type of motors, the dimensionless unit of time, used throughout the manuscript, roughly corresponds to $100ms$. We expect the induction motor and collective dynamics to reach an equilibrium in a fraction of a second to a few seconds. This is
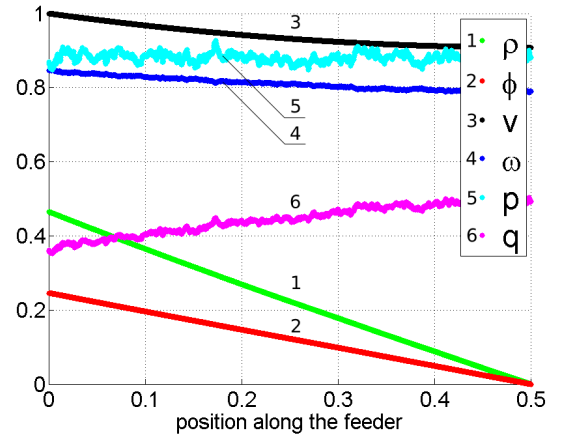

FIG. 3: Steady state profile along the feeder for all motors in the "normal" state for a sample of disorder drawn from the $\Delta = 0.0157$ and $z_d = 0.015$ for $v_0 = 1$. Notice, that while the disorder is clearly seen in active and reactive density consumptions p and q, its effect on ω, the flows ρ and ϕ, and the voltage v is significantly reduced.

shorter than the typical time for other discrete actions to occur (e.g. the disconnection of induction motors through their own thermal protective devices). Therefore, we expect our model to be valid over 30 msec to 3 sec timescales.

The dynamic simulations described in Section II D are used to find the initial steady profile using two simulation steps. Dynamic simulation is required because the state of the motors (see Fig. 2) is not known *a priori*. Disorder is initially ignored ($\Delta = 0$), v_0 is set to 1.0, ω is set to ω_0 and the steady (time-independent) solution of Eqs. (4-10) is found by integrating in time until the solution becomes stationary. This stationary solution is used as an initial condition for the next simulation. Using the same $\bar{\tau}_0$, disorder is re-introduced, and Eqs. (4-10) are again integrated until the solution becomes stationary. Fig. 3 shows a typical "normal" solution for a sample of disorder drawn from a distribution with $\bar{\tau}_0 = 0.9$, $\Delta = 0.0157$ and $z_d = 0.015$.

As clearly seen in Fig. 3 the effect of the disorder in τ_0 has little effect on ω but significantly larger effects on p and q. This is obviously the consequence of the structural properties of Eqs. (4,5,6). The relatively large effects of disorder on p and q is significantly diminished for ρ and ϕ because of the integral relationship between these variables in Eqs. (4, 5). The additional integral relationship in Eq. (6) further reduces the effect of disorder on v. It is important to note that the relatively small impact of disorder in Fig. 3 is a result of ω and v being large enough to be far from v_c^-, i.e. transition point for high voltage to low-voltage branch in Fig. 2. During the dynamic simulations, this transition region will often reside within the circuit and the relatively small disorder in τ_0 will be magnified by the step change in p, q, and ω across this transition.
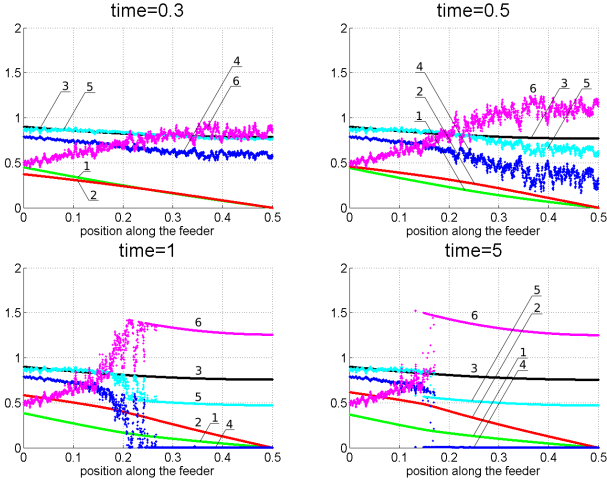
FIG. 4: Typical sequence of snapshots of the dynamics for "Case A—Stalling Front" for $\Delta = 0.0157$ and $z_d = 0.005$. The color of the lines is the same as in Fig. 3. As the stalling front passes from $z = L$ to lower z, the disorder in τ_0 interacts with the state transition in Fig. 2 to amplify the disorder in τ_0.

B. Case A—Stalling Front Dynamics

Starting from a steady-state condition solved using Case S, v_0 is suddenly lowered by a range of Δv's to initiate a front of motor stalling. Figure 4 displays the typical dynamics via a time series of snapshot of v, ρ, ϕ, ω, p, and q. The reduction of v_0 from 1 to 0.9 at $t = 0$ lowers v all along the circuit. The lower voltage reduces the electrical torque on all the motors and the disorder in the mechanical torques causes neighboring motors to decelerate at different rates creating a significant amount of disorder in ω even before any of the motors crosses the transition from a normal to a stalled state (see Fig. 4 at t=0.3). At $t = 0.5$, motors near the end of the line begin to stall, however, they all begin this transition at slightly different times because of the initial variability in their deceleration rates. The rapid deceleration during this transition significantly amplifies the disorder ω caused by the disorder in τ_0 The disorder also appear in q because of the large difference in q on either side of the transition. At $t = 1$, the the motors near the end of the circuit have completed their stalling transition and are all near $\omega = 0$ which suppresses the impact of the disorder in τ_0. The disorder in τ_0 is only amplified near the stalling front where significant dynamics are still occurring. At $t = 5$, the dynamics have essentially ceased. The disorder in τ_0 causes each motor to have slightly different v_c^- (see Fig. 2, and we believe that this variation in the transition threshold causes the majority of the residual disorder in ω and q.

The same reduction in v_0 is applied to one hundred samples of several different ensembles of disorder, i.e. different values of Δ and z_d. For each ensemble, the steady state values of $\rho(0)$, $\phi(0)$, and z_f are collected and binned into histograms. Gaussians are fit to these histograms, and the results are plotted in Fig. 5. We first consider the behavior of z_f, i.e. the probability distribution $\mathcal{P}(z_f)$. For each sample the value

of z_f is found via the average between the most left point in the "stalled" state and the most right one in the "normal" throughout the feeder. For a given correlation length z_d of the τ_0 disorder, the width of $\mathcal{P}(z_f)$ grows as Δ grows. (See the difference in the solid and dashed traces of the same color in Fig. 5). In fact, for each z_d, the width of $\mathcal{P}(z_f)$ approximately doubles for a doubling in Δ.

This effect appears to be local. Specifically, if Δ was zero, the front would stop in the same place z_f^0 for each sample. With variability in τ_0, i.e. $\Delta \neq 0$, the front might stall slightly earlier ($z_f > z_f^0$) if it encounters a small cluster of low τ_0 motors at slightly larger z_f. Or, it may stall slightly later ($z_f < z_f^0$) if there is a small cluster of high τ_0 motors near z_f^0 with cluster of low τ_0 motors at smaller z. The finite correlation length z_d ensure that such clusters will exist. These correlations could create nonlocal effects of disorder, however, we do not believe this is the case. In Figs. 4 and 5, the z_f are distant from the end of circuit compared to z_d. The relatively small z_d and the smoothing discussed in Section III A drastically reduce any residual effect of the disorder in τ_0 on the voltage profile with the result that the average position of z_f is nearly the same in all cases. However, at the larger z_d, there does appear to be a slight shift toward larger z_f although this result is not definitive.

The general trend is the same for the other two variables $\rho(0)$ and $\phi(0)$. However, this is expected because the final location of stalled front has a major influence over the motor loads which in turn create both $\rho(0)$ and $\phi(0)$.

Additional numerical experiments shed more light on the effects of disorder in τ_0 on the properties of the stalled front. In Fig. 6, simulations are performed for a fixed disorder ensemble (Δ=0.0079 and $z_d = 0.005$), but the reduction in v_0 is varied. As expected, for smaller v_0 the front stalls closer to the end of the circuit. However, the width of $\mathcal{P}(z_f)$ is larger than when the front stalls at smaller z (i.e. for larger reductions in v_0). The cause of this larger width is two-fold. First, the slope of $v(z)$ is smaller for $z \sim L$ making the position of the front much more susceptible disorder. Second, being closer to the end of the circuit provides less smoothing of v, and the correlation length z_d is more effective at causing variations in v near to the nominal location of stalling. The effects on $\mathcal{P}(\rho(0))$ and $\mathcal{P}(\phi(0))$ in Fig. 6 can be inferred from $\mathcal{P}(z_f)$ and Eqs. 4-5.

C. Case B—Restoration Front Dynamics

Fig. 7 show the snapshots of the dynamics for a restoration front. At t=1.1, v_0=0.8 and has been held at this low value long enough so that all of the motors on circuit have stalled. The disorder in τ_0 has little effect because all of the motors are stalled and are far from v_c^+, i.e. the transition to the normal state. Immediately following t=1.1, v_0 is raised back to 1.0 launching a recovery front into the circuit from z=0. The effect of the disorder is very similar to the stalling front. Specifically, at t=1.5, the motors beyond the front are just beginning to accelerate creating moderate disorder in ω because of the different rates of acceleration. Within the front, this disorder
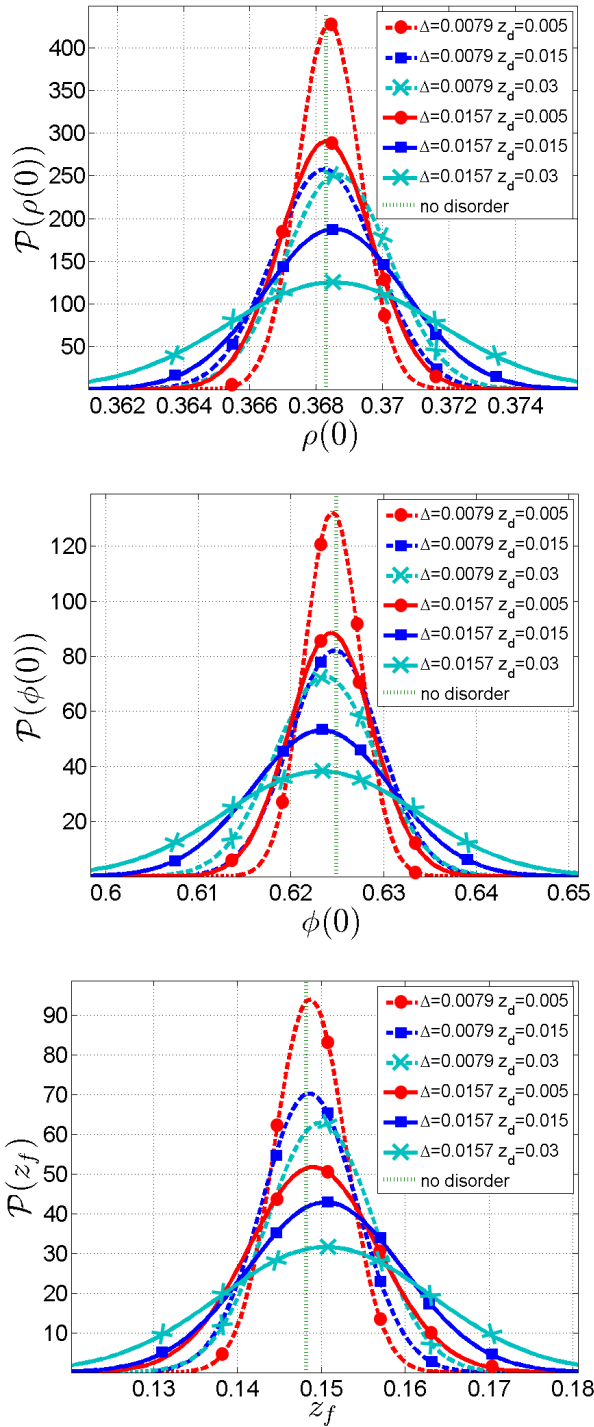
FIG. 5: Gaussian fits to the probability density distribution functions over $\rho(0)$, $\phi(0)$ and z_f after reaching steady state for Case A—Stalling front dynamics. Statistics are collected over 100 samples each disorder ensemble parameterized by Δ and z_d. The vertical dashed line indicates the position of the front for no disorder, i.e. Δ=0 and z_d=0.
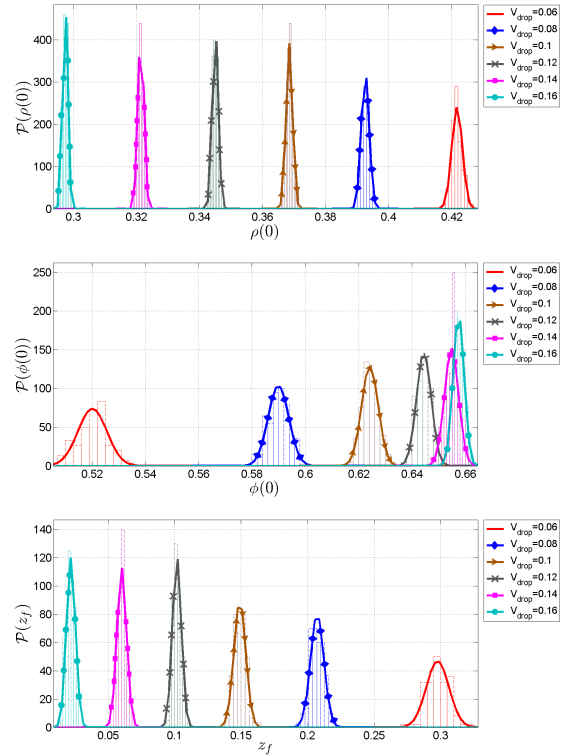

FIG. 6: Probability distribution functions over $\rho(0)$, $\phi(0)$ and z_f observed for the $\Delta = 0.0079$ and $z_d = 0.005$ ensemble after reaching steady state following Case A—Stalling front dynamics for different values of v_0.

is amplified during the rapid dynamical transition from the stalled to the normal state. For locations behind the front, i.e. small z, the disorder has limited effect on ω because the accelerations have mostly ceased. This behavior persists though the simulation up to t=6 when the front is nearly stationary. At these long times, the effect of the disorder is again local and static, i.e. disorder in τ_0 drives disorder in v_c^+ for each motor which manifests as randomness in the motor state near the stall restoration front.

The probability distribution $\mathcal{P}(z_f)$ for the steady-state z_f is shown in Fig. 8. The effect of disorder on $\mathcal{P}(z_f)$ is very similar to Case A–Stalling front dynamics. At fixed z_d, the width of $\mathcal{P}(z_f)$ approximately doubles when the amplitude of the disorder Δ doubles. Following a similar argument as in Section III B, we conclude that the effect of the disorder is primarily local and somewhat contingent on z_d, i.e. pockets of motors with high and low τ_0 that catch the restoration front early or allow it to propagate a bit further before becoming stationary. Fig. 8 does not show $\mathcal{P}(\rho(0))$ or $\mathcal{P}(\phi(0))$, but their relationship to $\mathcal{P}(z_f)$ is very similar to the relationship in Fig. 5.
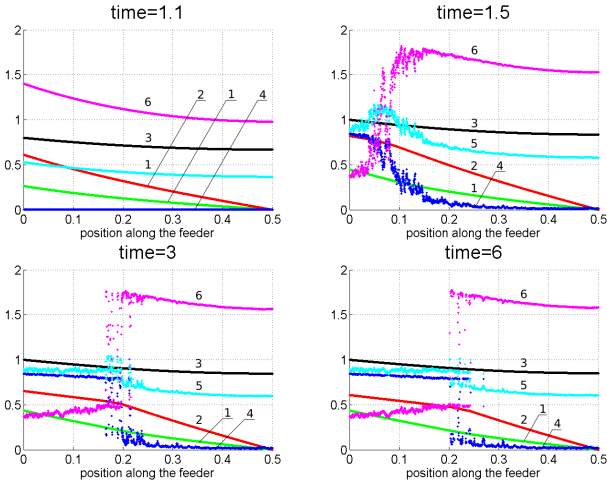
FIG. 7: Typical sequence of snapshots of the dynamics for "Case B—Restoration Front" for $\Delta = 0.0157$ and $z_d = 0.005$. The color of the lines is the same as in Fig. 3. As the restoration front passes from $z = 0$ into the circuit, the disorder in τ_0 interacts with the state transition in Fig. 2 to amplify the disorder in τ_0.
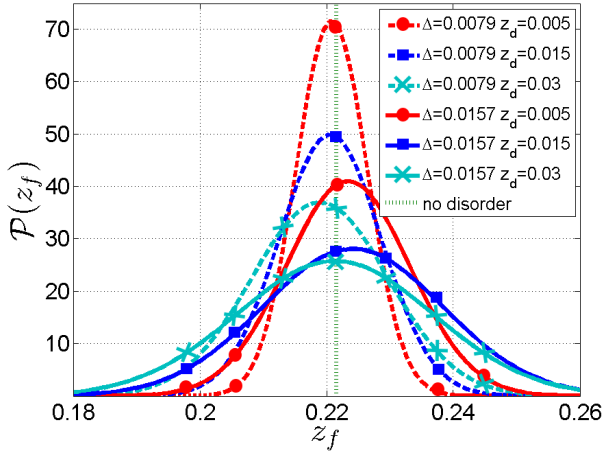

FIG. 8: Gaussian fits to the probability density distribution function over z_f after reaching steady state for Case B—Restoration front dynamics. Statistics are collected over 100 samples each disorder ensemble parameterized by Δ and z_d. The vertical dashed line indicates the position of the front for no disorder, i.e. $\Delta=0$ and $z_d=0$.

D. Case C—Fault Clearing

The dynamics of fault clearing is more complex than just a stalling front or a restoration front. In fault clearing, the circuit starts out in a steady state with $v_0=1$ and all of the motors in the normal state (see Fig. 2). At $t=0$, the v_0 is reduced to 0.9 and held low for time τ. After τ, v_0 is restored to 1.0 and the dynamics are simulated until the motors reach a steady state. A bisection search in τ is used to find τ_{cl}, i.e. the maximum clearing time where the motors at the end of the circuit will just recover. The circuit is considered "restored" even if there are just a few locations ($\sim$ 1-3) with stalled motors.

The search is carried out for 100 realizations of four disorder ensembles.

The distributions of τ_{cl}, i.e. $\mathcal{P}(\tau_{cl})$ are plotted in Fig. 9. In general, an increase in the amplitude of the disorder Δ results in a shift of $\mathcal{P}(\tau_{cl})$ to shorter τ_{cl} while an increase in the correlation length z_d of the disorder results in significant broadening of $\mathcal{P}(\tau_{cl})$. The complexity of the fault-clearing dynamics become evident by comparing the maximum clearing times in Fig. 9 with the snapshots of a stalling front in Fig. 4. The τ_{cl} are on the order of 0.3 to 0.5 in Fig. 9. Inspection of Fig. 4 at these times shows that the stalling front has not yet reached a steady state. In fact, none of the motors has even reached $\omega/\omega_0 \sim 0$. Before attempting to understand the effects of disorder on τ_{cl}, we first give a qualitative description of the fault-clearing dynamics.

A qualitative understanding of boundary between a "stalled" circuit, i.e. the occurrence of a FIVDR event, and a "recovered" circuit is gained by inspecting the snapshots of the dynamics in Fig. 4. This simulation corresponds to disorder parameterized by Δ=0.0157 and z_d=0.005, which is the same as the green curve in the upper plot of Fig. 9. Consider the t=0.5 snapshot in Fig. 4. The motors near the end of the circuit have $v \sim 0.75$ and $\omega/\omega_0 \sim 0.3$. If v_0 was restored to 1.0 at this time, the end of the line would at best have $v \sim 0.85$. In reality, it would be lower because the reactive power consumption of the motors would increase at the higher voltage. However, mapping the state $v \sim 0.85$ and $\omega/\omega_0 \sim 0.3$ onto the torque plot of Fig. 1, we find that the electrical torque falls below the mechanical torque. Therefore, even after the fault is cleared and v_0 is restored to 1.0, the motors at the end of the circuit will continue to decelerate. As they slow, their reactive power increases somewhat (see Eq. 5) which has a tendency to suppress the voltage further. The result is that, at t=0.5, the motors near the end of the circuit will continue to decelerate to near $\omega/\omega_0 \sim 0$ even after the fault is cleared—a conclusion consistent with the clearing time plots in Fig. 9.

At t=0.3 in Fig. 4, the situation is very different. The motors near the end of the circuit have only decelerated to $\omega/\omega_0 \sim 0.6$ and the local voltage is $v \sim 0.8$. If the fault was cleared at t=0.3, the voltage at the end of the circuit was jump up to about 0.9. Mapping the post-fault clearing state $\omega/\omega_0 \sim 0.6$ and $v \sim 0.9$ onto the torque curves in Fig. 1, we find that the electrical torque is safely above the mechanical torque, and even the motors at the end of the circuit is begin to accelerate after the fault is cleared. At higher ω/ω_0, their reactive power consumption decreases which reinforces the increase in voltage and the overall recovery.

From this qualitative description, we expect that the effect of disorder is primarily felt in the initial deceleration of the motor while the fault is applied rather than during post-fault recovery period. The spatially correlated disorder will result in clumps of motors with higher than average t_0. These motors will decelerate faster than an average motor pushing them to lower values of electrical torque along a constant v curve in Fig. 1. The tendency is for these motors to experience a decelerating net torque after fault clearing. The implication is that average maximum clearing times τ_{cl} become shorter and more broadly distributed.
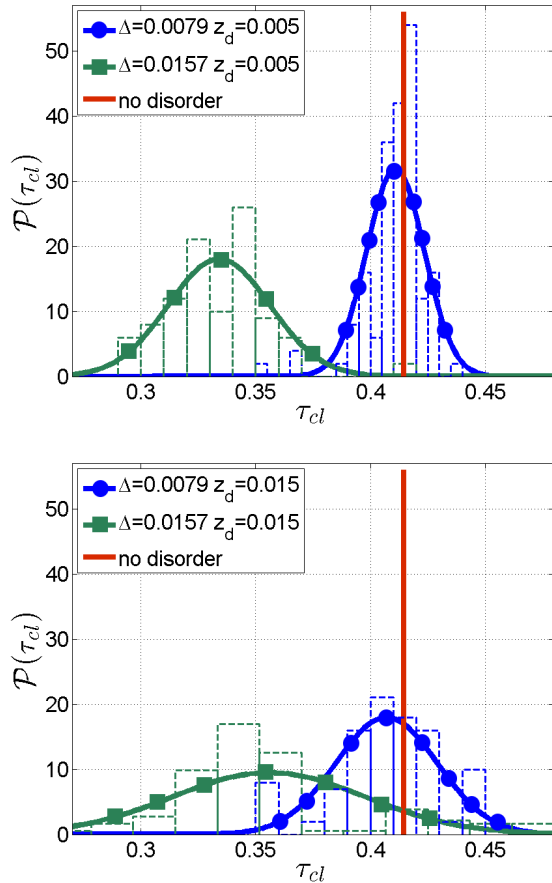
FIG. 9: Histograms and respective Gaussian fits for the probability density distribution function of the maximum clearing time, τ_{cl}, measured under experiments C for four different ensembles and for the case of no disorder (vertical red lines).

FIG. 10: Histograms and respective probability density distribution functions for the width of the burry regions, z_w, shown for the final state of the respective ensembles (see the legend) in experiments A and B.

E. Width of the blurry region

An interesting consequence of the disorder is seen in Fig. 10 where the probability density distribution function of the blurry region width, z_w is shown for different values of the disorder amplitude Δ and correlation length, z_d. We observe, in particular, that z_w increases with increase in Δ (when z_d is fixed) and decrease in z_d (when Δ is fixed). We postpone detailed discussions and explanations of this phenomenon for future publications.

IV. CONCLUSIONS AND PATH FORWARD

Loading on electrical distribution circuits is far from uniform and is often clumped into load pockets distributed along the circuit. To better represent the effect of these conditions on the distribution grid dynamics of induction motor loads, we have introduced an electrical load model that includes spatially-correlated load disorder. To investigate the effects of this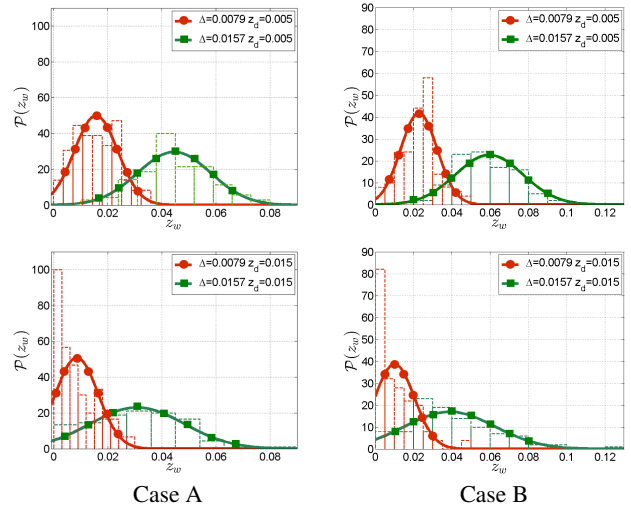 new loading, we have performed numerical simulation of the dynamics of a radial distribution circuit using this model of load disorder and explored the effect of disorder on the critical clearing time to avoid a Fault-Induced Delayed Voltage Recovery (FIDVR) event. Although the effects of disorder do bring new and important qualitative behaviors, by and large, the main qualitative picture of the front propagation phenomena observed in the spatially homogeneous case[1] remains the same but with some differences in the more complex dynamics of fault clearing. Specifically,

- For both stalling and restoration dynamics, the fronts propagate in time, slow down and eventually stop in a partially stalled state (for the right combinations of circuit length and voltage perturbation)

- For relatively small disorder, there is a threshold, i.e. a reasonably well defined maximum clearing time τ_{cl}, that separates the final circuit states into fully restored ($\tau < \tau_{cl}$) and only partially restored ($\tau > \tau_{cl}$).

- However, as the disorder becomes larger in amplitude with longer correlation lengths, the distribution of maximum clearing times becomes quite broad.

The broad distribution of maximum clearing times is likely related to new qualitative effects that emerge from the presence of disorder. Specifically, Figs. 4 and 7 both show that a group of motors with a distribution of mechanical torques undergoing acceleration or deceleration acquire a wide distribution of motor rotational frequencies. This effect is particularly evident in Fig. 4 at t=0.5. Motors with higher mechanical torque undergoing deceleration during a fault reach lower rotational frequencies and are in a more precarious situation. After fault clearing, they may not recover to normal rotational rate near grid frequency. Instead they may experience a net decelerating torque and stall. The effect of this local stalling on surrounding motors is still an unresolved questions.

There are many ways that this work could be extended and improved, including:

- Improving the load models by including spatially-distributed constant impedance, constant current, or constant power loads and investigating the effects of these combined loads on the induction motor dynamics.

- The exploration of analytical approximations to the maximum fault clearing time based on the qualitative description of post-fault recovery in Section III D.

- Extension of the model to distribution circuits with multiple branches and/or multiple circuits emanating from a single substation.

- The development of new controls to arrest a FIDVR event before it becomes established, possibly using distributed control of reactive power generation by customer-owned inverters [13].

We would also like to stress that validation of the detailed results provided by our model are difficult, and still unavailable, for several reasons, foremost is the lack of the appropriate data. Over the last several years, researchers and electrical utilities have dramatically improved the instrumentation of electrical grids, including the distribution circuits[14, 15] where some aspects of the dynamics explored here have been captured. However, these measurements have typically been at a single location along a distribution circuit, whereas the model developed in the manuscript explores spatially distributed and collective dynamical effects. To gain a full understanding of the dynamics that lead to FIDVR, we believe it is crucial for instrumentation to be installed at multiple locations along a many distribution circuits. The current instrumentation only monitors voltage and load. Instrumentation should be expanded to include power flows along the circuit. These expanded measurement configurations will help to disentangle individual motor dynamics from the collective dynamics of the entire distribution circuit. Finally, we conclude the manuscript briefly mentioning a related modeling work. A more complicated model that includes angular dependent mechanical torque and full electromagnetic modeling of the induction motors [16] has been developed. Similar to the current work, this model also shows the wave-like nature of the collective dynamics and partial stalling of a circuit with a interface between normally running and stalled motor. Although observed in two different models, we emphasize that this interface between stalled and normally running circuit sections has yet to be observed in utility data. To do so requires the expanded measurement configurations discussed above.

[1] C. Duclut, M. Chertkov, and S. Backhaus. Hysteresis, phase transitions and dangerous transients in power distribution systems. *Physical Review E*, 87:062802, 2013.

[2] B. Lesieutre, R. Bravo, R. Yinger, D. Chassin, H. Huang, N. Lu, I. Hiskens, and G. Venkataramanan. Load modeling transmission research. Technical report, LBNL, 2010.

[3] D Kosterev, B. Yinger, J. Shaffer, G. Bullock, T. Gentile, I. Grant, B. Taylor, L. andJones, T. Cain, R. Bottoms, J. Shultz, J. Mitsche, J. Loock, J. Eto, G. Kobet, and Agrawal B. Fault-induced delayed voltage recovery. Technical report, NERC, 2009.

[4] L. Pereira, D. Kosterev, P. Mackin, D. Davies, J. Undrill, and Wenchun Zhu. An interim dynamic induction motor model for stability studies in the wscc. *Power Systems, IEEE Transactions on*, 17(4):1108 – 1115, nov 2002.

[5] B.R. Williams, W.R. Schmus, and D.C. Dawson. Transmission voltage recovery delayed by stalled air conditioner compressors. *Power Systems, IEEE Transactions on*, 7(3):1173 –1181, aug 1992.

[6] J.W. Shaffer. Air conditioner response to transmission faults. *Power Systems, IEEE Transactions on*, 12(2):614 –621, may 1997.

[7] M. Chertkov, S. Backhaus, K. Turtisyn, V. Chernyak, and V. Lebedev. Voltage Collapse and ODE Approach to Power Flows: Analysis of a Feeder Line with Static Disorder in Consumption/Production. *http://arxiv.org/abs/1106.5003*, 2011.

[8] J.S. Thorp, C.E. Seyler, and A.G. Phadke. Electromechanical wave propagation in large electric power systems. *Circuits and Systems I: Fundamental Theory and Applications, IEEE Transactions on*, 45(6):614 –622, June 1998.

[9] M. Parashar, J.S. Thorp, and C.E. Seyler. Continuum modeling of electromechanical dynamics in large-scale power systems. *Circuits and Systems I: Regular Papers, IEEE Transactions on*, 51(9):1848 – 1858, 2004.

[10] Danhua Wang, K. Turitsyn, and M. Chertkov. Distflow ode: Modeling, analyzing and controlling long distribution feeder. In *Decision and Control (CDC), 2012 IEEE 51st Annual Conference on*, pages 5613–5618, Dec 2012.

[11] D.H. Popovic, I.A. Hiskens, and D.J. Hill. Stability analysis of induction motors network. *Electrical Power and Energy Systems*, 20(7):475–487, 1998.

[12] T.-F. Chan and K. Shi. *Applied Intelligent Control of Induction Motor Drives*. John Wiley & Sons, 2011.

[13] K. Turitsyn, P. Sulc, S. Backhaus, and M. Chertkov. Options for control of reactive power by distributed photovoltaic generators. *Proceedings of the IEEE*, 99(6):1063 –1073, june 2011.

[14] R. J. Bravo and S. Robles. 2012 fidvr events analysis: Valley distribution circuits. 07/2013 2013. Prepared for Lawrence

Berkeley National Laboratory by Southern California Edison Advanced Technology, Engineering; Technical Services.

[15] R. J. Bravo and S. Robles. 2013 fidvr events analysis on valley distribution circuits. 12/2013 2013. Prepared for Lawrence Berkeley National Laboratory by Southern California Edison Advanced Technology, Engineering; Technical Services.

[16] Y. Liu, V. Vittal, J. Undrill, and J. H. Eto. Transient model of air-conditioner compressor single phase induction motor. *IEEE Transactions on Power Systems*, 28:4528–4536, 11/2013 2013.